



Highly-efficient photocatalytic H₂O₂ evolution using hydrothermal carbons with donor-acceptor furan couples

Wei Miao^a, Ducheng Yao^a, Chengcheng Chu^a, Ying Liu^a, Qisu Huang^a, Shun Mao^{a,*}, Kostya (Ken) Ostrikov^b

^a College of Environmental Science and Engineering, Biomedical Multidisciplinary Innovation Research Institute, Shanghai East Hospital, State Key Laboratory of Pollution Control and Resource Reuse, Tongji University, 1239 Siping Road, Shanghai 200092, China

^b School of Chemistry and Physics and QUT Centre for Materials Science, Queensland University of Technology (QUT), Brisbane, QLD 4000, Australia

ARTICLE INFO

Keywords:

Photocatalysis
H₂O₂ evolution
Hydrothermal carbonation carbon
Furan resin
Alternating donor-acceptor unit

ABSTRACT

Nature-inspired photosynthesis of H₂O₂ using sustainable catalytic materials is promising to generate high-value chemicals and solar fuels from renewable energy sources. However, existing H₂O₂ evolution systems still face limitations of low efficiency, high cost, and the need for sacrificial agents or organic electron donors. Herein, we report novel furan-resin-structured hydrothermal carbons (HTCs) as photocatalytic H₂O₂ generation catalysts by one-step hydrothermal carbonization of saccharides or biomass. The catalysts have high production efficiency (480.7 μmol g_{cat}⁻¹ h⁻¹) for photocatalytic H₂O₂ evolution without any sacrificial agent or O₂ aeration. This is one of the pioneer studies of HTCs constructed by low-bandgap furan resin comprising conjugated quinoid and aromatic furan units. The underlying mechanism is based on the π-stacked donor-acceptor (D-A) furan couples that significantly enhance the charge transfer efficiency of photogenerated electrons. The reported low-cost and easy-to-manufacture HTC photocatalysts with remarkable activity show great potential in artificial photosynthesis applications.

1. Introduction

Hydrogen peroxide (H₂O₂) has been widely used in chemical industry, medicine, and environmental remediation [1]. Considering the high energy consumption and chemical waste of the anthraquinone process, more economical and environmentally-friendly H₂O₂ production methods, e.g., electrocatalytic and photocatalytic oxygen reduction reaction (ORR), have attracted great attention in recent years [2]. Using renewable solar energy for clean production of H₂O₂ is particularly promising to reduce the associated carbon emissions. However, inefficient conversion of H₂O and O₂ into H₂O₂ is still one of the main obstacles for the photocatalytic H₂O₂ production. Therefore, the development of inexpensive, efficient, and environmentally-friendly catalysts is a critical challenge for photocatalytic H₂O₂ generation by artificial photosynthesis [3,4].

TiO₂ and carbon nitride (C₃N₄) are the most common photocatalysts for H₂O₂ production [5–8]. However, up to now, they still suffer from common problems including complex synthesis, expensive precursor, limited visible light absorption, need of sacrificial agent, oxygen

aeration, and acidic pH condition [9,10]. Recently, resorcinol-formaldehyde (RF) resin was utilized as a metal-free semiconductor photocatalyst for H₂O₂ production [11]. This new class of polymers consist of benzenoid structure as electron donor (D) and quinoid structure (resorcinol) as acceptor (A). The copolymerization of D-A couples through π-conjugation and inter-chain π-stacking results in the hybridization of low HOMO-LUMO gaps and creates a band gap (*E_g*) [12,13]. The reported conjugated D-A polymers can absorb broad-wavelength light up to ~700 nm and are conducive to water oxidation and oxygen reduction by the photogenerated charges [14]. Moreover, the surface chemistry and band structure of conjugated D-A polymer photocatalysts can be modulated, which offer a lot of possibilities in advanced photocatalysts for H₂O₂ production [15].

Hydrothermal carbonation carbon (HTC) is a metal-free polymer semiconductor with intrinsic chemical complexity and amorphous nature [16,17]. HTC is composed of a polyfuran skeleton with *sp*²-hybridization units, which can generate photoexcited electron-hole pairs under illumination. It is proposed that the photocatalytic activity of HTC is due to repeated furan units in a simple linear structure [18,19].

* Corresponding author.

E-mail address: shunmao@tongji.edu.cn (S. Mao).

<https://doi.org/10.1016/j.apcatb.2023.122770>

Received 27 October 2022; Received in revised form 10 April 2023; Accepted 12 April 2023

Available online 13 April 2023

0926-3373/© 2023 Elsevier B.V. All rights reserved.

However, another structure with conjugated furan pairs linked through $-CH_2$ group and C double bond has been proposed for HTC more than a decade ago [20]. Recently, the presence of such structure on the interface “shell” regions of HTC sphere has been demonstrated through scanning transmission X-ray microscopy (STXM) [21]. In particular, this structure is similar to the copolymerization of electron donor (D) and acceptor (A) monomers in low-bandgap polymer [11,13,22]. Although H_2O_2 production using HTC photocatalyst has been reported recently [23]. To the best of our knowledge, the HTC catalyst constituted by the π -stacked D-A furan couples has not been reported for photocatalytic H_2O_2 production, which motivated this work to explore its performance in H_2O_2 production. Moreover, HTC can be produced through saccharides and waste biomass conversion. In this regard, HTC is an ideal candidate catalyst for large-scale photocatalytic H_2O_2 production. However, the intermediates and precursors that constitute HTCs with photocatalytic activity are still not clearly identified, which limit the further development of HTCs in photocatalytic applications.

Here we synthesized 12 types of HTCs by one-step hydrothermal carbonization of saccharides including glucose (GLU), sucrose (SUC), and 5-hydroxymethylfurfural (HMF), fructose (FRU), lactose (LAC), maltose (MAL), and cyclodextrin (CYC), sodium alginate (ALG), and ascorbic acid (ASC) and biomass wastes including cellulose, bean straw, and rice straw. Surprisingly, most of the prepared HTCs exhibit unexpectedly high photocatalytic performance for H_2O_2 production without any sacrificial agent and O_2 aeration [24–27]. Importantly, we revealed the mechanisms of photocatalytic activity and formation of photoinduced H_2O_2 and related them to the unique polyfuran HTC structure. The results clearly show that the alternating electron donor (D) and acceptor (A) monomers in the chain of the furan resin enhance the charge transfer efficiency of photogenerated electrons, which is the main reason for the high activity of HTC in photocatalytic H_2O_2 generation. Moreover, we demonstrate the continuous generation of H_2O_2 in the scaled-up photocatalytic flow reactor system driven by a peristaltic pump. The HTC catalyst shows the remarkably high stability in long-time operation (24 hr), indicating the significant potential of HTC in large-scale H_2O_2 production. Collectively, this work reports a new type of high-performance H_2O_2 evolution catalysts and the underlying photocatalytic mechanisms. The reported HTC with the unique D-A couple contributes to the development of next-generation of low-cost, metal-free, and environment-friendly catalysts for a broader range of photo-chemical applications.

2. Experimental section

2.1. Preparation of HTCs

To prepare HTC, typically, 2 g of precursor was dissolved in 30 mL water. Then, the solution was heated at 200 °C in a Teflon-lined stainless autoclave for 12 h. Subsequently, the solution obtained after the reaction was centrifuged to obtain a solid product, which was then washed with pure water and ethanol. The obtained solid catalyst was dried in a vacuum oven at 60 °C for 24 h to obtain HTC. For HTCs prepared by rice straw and bean straw, 2 g of chopped rice straw or bean straw was added in 30 mL water and heated at 160 °C in a Teflon-lined stainless autoclave for 24 h to remove the impurities. The solid product was obtained by centrifugation. Then, the purified product was immersed in 30 mL water and heated at 200 °C in a Teflon-lined stainless autoclave for 12 h. Finally, the obtained solid products were washed with pure water and ethanol to obtain R-HTC (rice straw precursor) and B-HTC (bean straw precursor).

2.2. Photocatalytic production of H_2O_2

The H_2O_2 production experiments were conducted with a top illumination excitation setup. The batch reactor is a quartz beaker with 2 cm inner diameter, 5 cm height, 0.1 cm wall thickness, and 12.56 cm²

illumination area. The spiral photocatalytic flow reactor was made of a spiral quartz tube, which has 0.8 cm inner diameter, 11 cm height, 0.1 cm wall thickness, and 276.32 cm² illumination area. At first, 5 mg of the catalyst was dispersed in 50 mL water and sonicated and stirred for 15 min. Then, a 300 W LED white light (CEL-PE300-4A) with a 420 nm cutoff filter was used as the light source. Unless otherwise specified, the experiment conditions including the control experiments in this study are: water (50 mL), catalyst (5 mg), white LED light (> 420 nm, light intensity: 100 mW cm⁻²). During the reaction, the solution was stirred without pumping O_2 and 2 mL of sample was collected and filtered using a 0.22 μ m Millipore filter membrane at 10 min interval. The concentration of H_2O_2 was determined by the iodometric titration method with a UV-vis spectrophotometer. Typically, 2 mL of the reaction solution was taken and the photocatalyst was removed by filtration. Then, 1 mL of 0.4 M potassium iodide and 1 mL of 0.1 M potassium hydrogen phthalate ($C_8H_5KO_4$) were added. After standing for 30 min, the absorbance of the solution was measured at 350 nm using the ultraviolet visible spectrophotometer.

2.3. Photoelectrochemical measurements

Photoelectrochemical measurements were performed on CHI760D electrochemical workstation using a three-electrode cell, including saturated calomel electrode as reference electrode and Pt wire as counter electrode. Na_2SO_4 (0.1 M) was used as the electrolyte. 5 mg catalysts were dispersed into 4.25 mL H_2O , 4.25 mL isopropanol, and 0.5 mL of 5 wt% Nafion solution. Then, the mixture was sonicated to form a uniform ink. The working electrode was prepared by dip-coating the suspension (100 μ L) on tin oxide (ITO) glass electrode (1 \times 1 cm) and subsequently heated at 100 °C for two hours. Electrochemical impedance spectroscopy (EIS) was carried out at the open-circuit potential. For the rotating disc electrode (RDE) tests, 3 μ L suspension was put onto the glassy carbon electrode and dried for the test. The other experimental details and calculation methods can be found in the [Supplementary Data](#).

3. Results and discussion

3.1. HTCs with furan resin structure

Glucose (reducing monosaccharide) and sucrose (nonreducing disaccharide) are two of the common precursors for hydrothermal carbonization of HTC [28,29]. The 5-hydroxymethylfurfural (HMF) is an important intermediate and product in the hydrothermal reaction of saccharides. [28] Herein, glucose, sucrose, and 5-hydroxymethylfurfural were hydrothermally carbonized to produce the HTC catalysts (Fig. 1a). Previous studies on the synthesis process of HTC have proven that saccharides (monosaccharide and disaccharide) can be hydrolyzed into HMF under hydrothermal condition (≥ 180 °C). The HMF forms nano-sized particles through a polycondensation process. In this process, the primary nanoparticles aggregate to form carbonaceous spheres, which possess a complex carbon scaffold composed of polyfuran network and aromatic arene rings [17,28]. So far, there is no perfect model to represent the exact structure of HTC. The solid-state ¹³C nuclear magnetic resonance (NMR) study verified that 60% of the carbon atoms formed a network of furan motifs [30]. As shown in Fig. 1a, the α -carbons of two adjacent furanic rings are connected through $-CH_2$ group and C double bond, which constitute the structural unit composed of aromatic furan and quinoid furan. The alternating electron donor (D) and acceptor (A) monomers, i.e., the aromatic furan and quinoid furan, in the chain of furan resin can induce intramolecular charge transfer (CT) between the furan units [31]. As illustrated in Fig. 1a, when the D-A units are π -stacked on each other, the hybrid energy level contributes a direct bandgap of HTC.

As shown in Fig. 1b, the synthesized G-HTC particles show a spherical shape with a diameter of 200–300 nm; while the S-HTC and H-HTC

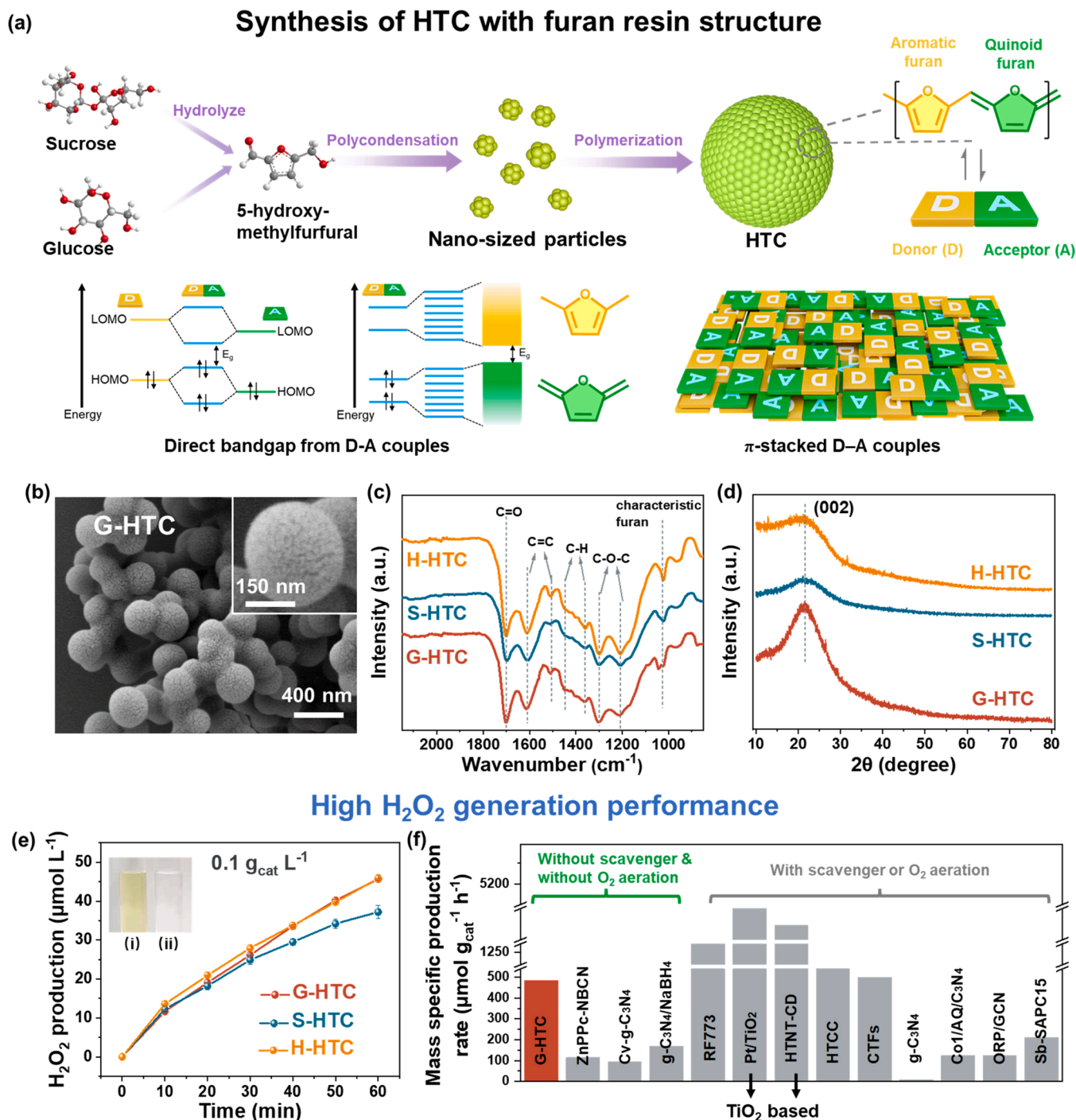


Fig. 1. HTCs with furan resin structure show high photocatalytic H₂O₂ production performance without scavengers or O₂ aeration. (a) Schematic of the synthesis process of HTCs. The fundamental furan structure and electronic structures of π -stacked D-A couples in HTC. (b) SEM images, (c) FT-IR spectra, and (d) XRD spectra of G-HTC, S-HTC, and H-HTC. (e) The photocatalytic H₂O₂ production performance of G-HTC, S-HTC, and H-HTC. Inset shows the chromogenic phenomenon (iodimetry test) of the reaction solution (i) before and (ii) after the addition of catalyst. Test conditions: water (50 mL), catalyst (5 mg), white LED light (> 420 nm, light intensity: 100 mW cm⁻²). (f) The comparison of H₂O₂ production performance with reported photocatalysts (more details are listed in Table S2).

particles show a similar morphology with the larger size (average diameter of 1.16 μ m for S-HTC and 368 nm for H-HTC, Fig. S1). Due to the disaccharide nature of sucrose, the large amount of decomposed species under hydrothermal conditions lead to the large diameter of the S-HTC microspheres [32]. The Brunauer–Emmett–Teller (BET) analysis results (Fig. S2) show that the specific surface area and total pore volume of G-HTC is 9.12 m² g⁻¹ and 1.90 $\times 10^{-2}$ cm³ g⁻¹, respectively, which indicates that the G-HTC nanospheres feature a very low pore abundance, and can be considered as non-porous particles.

The Fourier transform infrared (FT-IR) spectroscopy was used to analyze the chemical structure of the prepared HTCs. As shown in Fig. 1c, the band at 1701 cm⁻¹ is attributed to the stretching vibrations of C=O (the quinone groups link to the benzene ring, carbonyl, ester, or carboxyl). The bands located at 1608 and 1510 cm⁻¹ are assigned to C=C vibration and furanic rings, respectively [33]. The band at 1447 cm⁻¹ is ascribed to the methylene linker (C-H); while the band at 1362 cm⁻¹ corresponds to the stretching vibrations of C-H in the carbonyl [29]. The bands positioned at 1302 and 1207 are attributed to

the C–O–C stretching vibration. The 1021 cm^{-1} band is the characteristic band of furan ($1030\text{--}1015\text{ cm}^{-1}$) [18,34]. There is no noticeably significant difference between the spectra of three HTC samples, indicating that the synthesized HTC samples have the similar surface functional groups.

Based on the X-ray photoelectron spectroscopy (XPS) results (Fig. S3), carbon and oxygen elements were identified and the surface O/C atomic ratios of the prepared HTCs are summarized in Table S1. As shown in Fig. S4, the O 1s spectrum was deconvoluted into two characteristic peaks at 531.9 and 533.1 eV, which are assigned to C–O and C=O group, respectively [35]. Based on the FT-IR and XPS analysis, the different HTC samples possess similar contents of oxygen functionalities on the surface. The X-ray diffraction (XRD) patterns of the three HTC samples are shown in Fig. 1d. For all the HTC samples, only one broad diffraction peak is found at 21.5° . This peak is indexed to the (002) plane of amorphous graphitic carbon, which originates from the π -stacked polyfuran between D-A couples [36]. The S-HTC shows the weakest (002) peak, which indicates the lowest content of π -stacked D-A units in its structure [37]. To further study the graphitic carbon structure of HTC, as shown in Fig. S5, the solid-state electron spin resonance (ESR) spectra of G-HTC were measured. The spectra exhibit a Lorentzian line shape with the g value of 2.003, which originates from the delocalized π -electrons in the sp^2 -hybridization structure [38,39].

As photocatalyst for H_2O_2 evolution (Fig. 1e), without the addition of sacrificial agent or purging oxygen, the G-HTC, H-HTC, and S-HTC samples all exhibit a high H_2O_2 production performance. The inset of Fig. 1e shows the chromogenic phenomenon of the solution after the photocatalytic reaction. The reacted solution showed a bright yellow color in the iodimetry test, indicating the formation of H_2O_2 . In contrast, when catalase was added, the solution became colorless due to the effective consumption of H_2O_2 . As shown in Fig. 1f, modified TiO_2 [10] and C_3N_4 are the representative catalysts for photocatalytic H_2O_2 production. As a new type of semiconductor photocatalyst, the G-HTC exhibits excellent H_2O_2 evolution performance without sacrificial agent or oxygen aeration, even better than some of the systems using sacrificial

agent or oxygen aeration (Table S2) [24,25,27,40–47]. Compared with other metal-free polymer photocatalysts, the reported HTCs possess the advantages of low cost and easy preparation. Considering that the surface engineering at the molecular level of metal-free polymer can further boost the photocatalytic performance, the unmodified HTCs reported in this study have great potentials.

3.2. Optical properties and electronic band structures of HTCs

The optical properties of the synthesized HTC catalysts were first studied by the diffuse reflectance UV–vis spectra (DRS). The intrinsic semiconductor absorption of all HTCs is observed over the whole visible light region (Fig. 2a). The bandgaps from the Tauc plots were calculated to be 2.09 eV, 2.00 eV, and 1.96 eV for G-HTC, S-HTC, and H-HTC, respectively (Fig. 2a, inset). Fig. S6 shows the Mott-Schottky plots of the HTCs with the frequencies of 0.5, 1.0, and 1.5 kHz. The conduction band (CB) positions of the HTCs versus RHE at pH 0 were calculated by the Mott-Schottky plots (calculation details in Supplementary Data). Based on the obtained bandgap values, the CB positions of the G-HTC, S-HTC, and H-HTC samples were calculated to be -0.41 V , -0.48 V , and -0.39 V (vs RHE), respectively. Fig. 2b shows the complete band structures of the three HTCs. Remarkably, both the redox potentials of $\text{O}_2/\text{O}_2^{\cdot-}$ (-0.33 V vs RHE) and $\text{O}_2/\text{H}_2\text{O}_2$ ($+0.68\text{ V}$ vs RHE) are within the energy band of the HTCs. This suggests that both the one-step and two-electron O_2 reduction processes can be effectively driven by this HTC-based photocatalytic system under visible light thermodynamically. It is also noticed that the valence band of HTC is above $\text{O}_2/\text{H}_2\text{O}$ ($+1.23\text{ V}$ vs RHE), indicating the ability of HTC to oxidize water to produce oxygen (water oxidation reaction, WOR). As shown in Fig. S7, the role of electrons and holes during the photocatalytic process with G-HTC catalyst is illustrated in the schematic diagram. In addition, the specific extinction coefficients of G-HTC, H-HTC, and S-HTC were determined as 0.079, 0.077, and $0.079\text{ m}^2\text{ g}^{-1}$, respectively, by the average value of specific extinction coefficients at different wavelengths and with

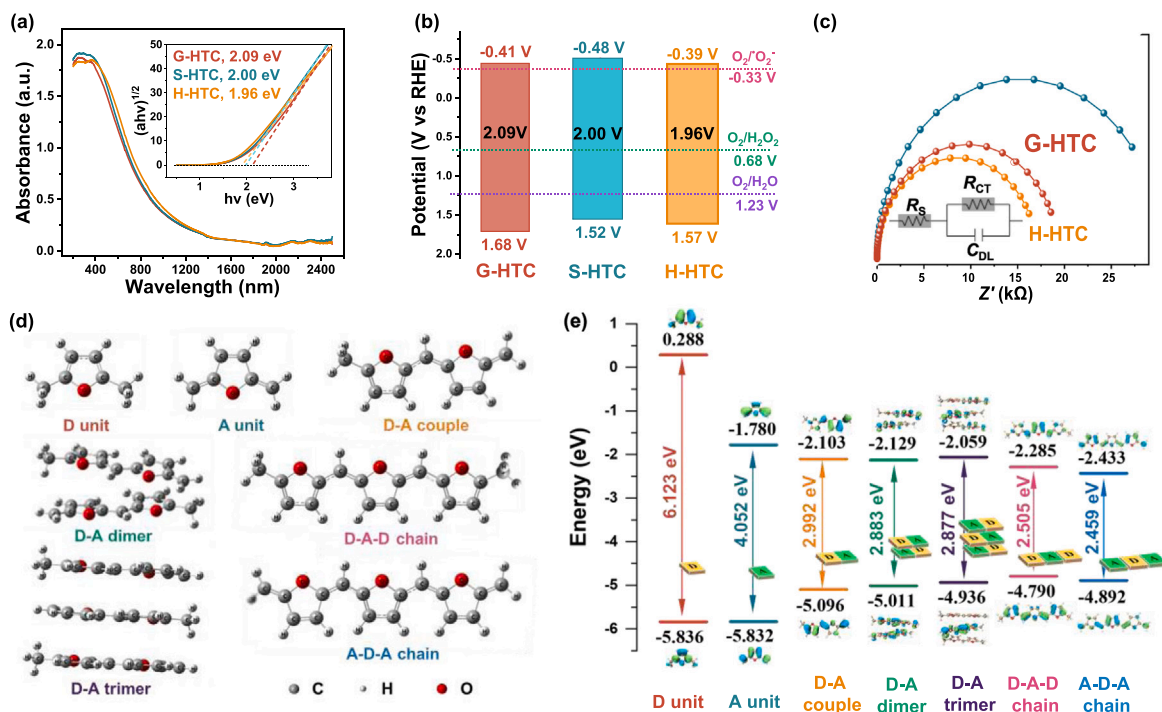


Fig. 2. Optical properties and electronic band structures underpin the photocatalytic activity of HTCs. (a) UV–vis DRS of G-HTC, S-HTC, and H-HTC. Inset shows the corresponding plots of transformed Kubelka–Munk function versus photon energy. (b) The band structure alignments and (c) EIS Nyquist plots of G-HTC, S-HTC, and H-HTC. Inset is the equivalent circuit. (d) Optimized structures of “D”, “A”, “D-A couple”, “D-A dimer”, “D-A trimer”, “D-A-D chain”, and “A-D-A chain” models. (e) The energy diagrams and interfacial plots of π -stacked D-A structures.

different catalyst concentrations [48]. The specific extinction coefficients further indicate that the three photocatalysts have almost the same light absorption capacity (Supplementary data and Fig. S21) [49].

The electrochemical impedance spectra (EIS) were measured to investigate the conductivity and charge migration rate of the photocatalyst. As shown in Fig. 2c, G-HTC and H-HTC show a similar radius of the arc, and S-HTC possesses a larger CT resistance (R_{CT}), which is consistent with the weakest π -stacked D-A furan-based units in its structure [36]. To be specific, the π -stacked D-A structures result in low R_{CT} , which contributes to the faster interfacial charge separation, electron transfer, and higher photocatalytic activity [50]. The transient photocurrent response under visible-light irradiation was tested for HTC coated fluorine tin oxide (FTO) electrodes, which confirmed the effective separation of photoexcited charge carriers (Fig. S8) [51,52].

Considering the positive correlation between the HOMO-LUMO gaps and the optical band gap obtained from the UV-vis-NIR spectra, the electronic properties of the polyfuran network in HTC were further investigated with simulation models including aromatic furan (D), quinoid furan (A), D-A couple, π -stacked D-A dimer, π -stacked D-A trimer, D-A-D chain, and A-D-A chain (Fig. 2d). The energy levels of these models were studied by the density functional theory (DFT) simulation (details in Supplementary Data). As shown in Fig. 2e, the charge transfer interaction of the D-A couple creates the smaller HOMO-LUMO gap (2.992 eV) compared to those of the aromatic furan (4.052 eV) and quinoid furan (6.123 eV). Moreover, it is found that the HOMO-LUMO gaps of the π -stacked D-A dimer (2.883 eV) and π -stacked D-A trimer (2.877 eV) are even smaller than that of the D-A couple. Generally, the HOMO-LUMO gap of oligomers can be used to measure the conductivity of molecules, and the smaller the HOMO-LUMO gap the better the conductivity [53]. The DFT simulation also shows that when the D-A couple is extended to D-A-D or A-D-A chain, the HOMO-LUMO gap is further reduced to 2.505 eV and 2.459 eV, respectively. Thus, it is reasonable to expect that the π -stacked D-A chains with repeating D-A furan units have a low bandgap semiconductor structure. These results clearly indicate that the π -stacked assembly of the donor-acceptor furan couples can extend π -delocalization, which leads to the low-bandgap semiconductor structure [11], thereby benefiting the HTC

photocatalytic activity for H_2O_2 evolution.

3.3. Photocatalytic activity of HTCs

The G-HTC was used as a representative catalyst in photocatalytic H_2O_2 evolution study. At first, the apparent quantum yield (AQY) of G-HTC (details in Supplementary Data and Table S3) under monochromatic light irradiation at 420 nm, 475 nm, 550 nm, and 600 nm was determined as 0.677%, 0.285%, 0.216%, and 0.168%, respectively (Fig. 3a). Moreover, under simulated sunlight irradiation, the solar-to- H_2O_2 (STH) energy conversion efficiency for H_2O_2 generation reaches 0.051% (details in Supplementary Data). This reveals that the broad-spectrum light absorption by G-HTC is beneficial for the highly-efficient H_2O_2 generation. The working condition, e.g., the atmosphere, has a major impact on the photocatalytic H_2O_2 generation performance. As shown in Fig. 3b, a sharp increment of the photocatalytic H_2O_2 production is observed in O_2 -saturated DI water, confirming that O_2 is a pivotal factor in the photocatalytic reaction. Nevertheless, a small yield of H_2O_2 is still achieved in Ar-saturated solution, indicating that the photogenerated valence band holes ($VB h^+$) can decompose water to produce O_2 (Eq. (1)):



The H_2O_2 production experiments were conducted with a top illumination setup in a planar reactor, and the reactor thickness was fixed at 3.5 cm. The optimum range for radiation absorption (optical thickness) in a planar photoreactor was reported as 4.1–4.4 [54,55]. According to the calculation formula of optical thickness, the optimal catalyst concentration was therefore determined as 0.148–0.158 g L⁻¹ in our experimental setup. Fig. 3c shows the mass specific production rate and H_2O_2 production rate by G-HTC with different catalyst loadings (0.1, 0.15, 0.2, and 0.3 g L⁻¹). Although the H_2O_2 production rate increases with the increase of catalyst loading, the mass specific production rate of G-HTC reaches the highest value of 480.7 $\mu\text{mol g}_{\text{cat}}^{-1} \text{h}^{-1}$ at the optimal concentration of 0.15 g L⁻¹. The above results indicate that the H_2O_2 production rate is also determined by the catalyst concentration and optical thickness in the reactor in addition to the wavelength and

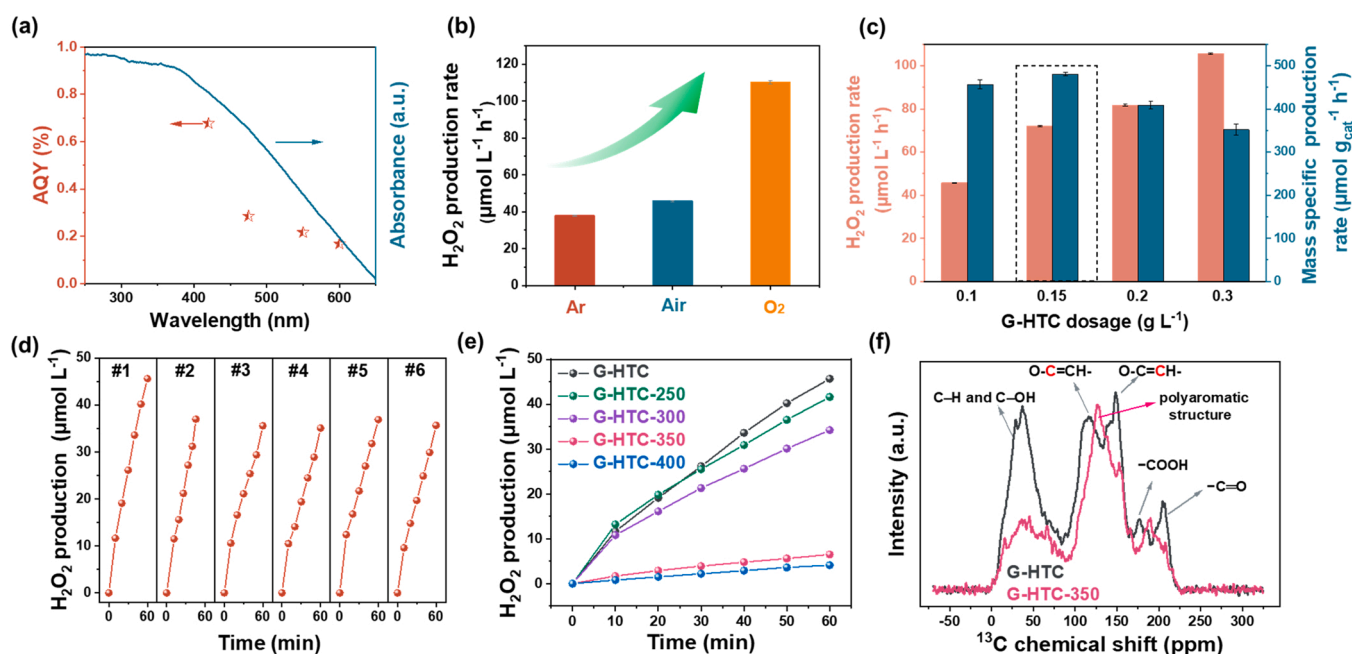


Fig. 3. Photocatalytic activity of G-HTC for H_2O_2 production. (a) The AQY of G-HTC for H_2O_2 production. (b) Effect of dissolved oxygen on the photocatalytic production of H_2O_2 . (c) The H_2O_2 production rate and mass specific production rate with different catalyst dosages (0.1–0.3 g L⁻¹) in air. (d) Cycle test of photocatalytic H_2O_2 generation with G-HTC. Test conditions: water (50 mL), catalyst (5 mg), white LED light (> 420 nm, light intensity: 100 mW cm⁻²). (e) The performance of G-HTC and pyrolyzed G-HTC for photocatalytic H_2O_2 production. (f) Solid-state ^{13}C NMR spectra of G-HTC and G-HTC-350.

intensity of light source. In addition, the macroscopic changes in the light intensity before and after passing through the reactor indicate that most of the radiation energy have been absorbed at the catalyst loading of 0.1–0.3 g L⁻¹ (Table S4) [56,57].

The formation and decomposition of H₂O₂ with the G-HTC catalyst were further investigated by the kinetics study. The formation and decomposition rates follow the zero-order and first-order kinetics toward H₂O₂, respectively, which can be obtained by the following Eq. (2):

$$[H_2O_2] = (k_f/k_d) / \{1 - \exp(-k_d t)\}, \quad (2)$$

where k_f is the formation rate constant (μmol·L⁻¹·min⁻¹) and k_d (min⁻¹) is the decomposition rate constant. As shown in Fig. S9, with 2.0 g L⁻¹ G-HTC, the k_f was only increased by 2.19 times under the oxygen aeration condition compared with that without oxygen aeration. The results confirm that although O₂ is a key factor in the photocatalytic reaction, the production of H₂O₂ is not solely determined by the partial pressure of O₂. The decomposition reaction of H₂O₂ on the catalyst surface will affect the apparent concentration that can be detected experimentally.

The recyclability and stability of G-HTC in photocatalytic production of H₂O₂ were further tested. As shown in Fig. 3d, the G-HTC catalyst shows a 18.9% decline of H₂O₂ production rate after the 1st cycle, and is then stabilized in the subsequent cycles. The drop of H₂O₂ production rate after the first cycle is possibly due to the persistent free radicals (PFRs) of fresh HTC catalysts, which can react with O₂ and produce H₂O₂ and •OH [58]. As shown in Fig. S10, when the organic solvent extracting technique was used to eliminate the PFRs in the fresh G-HTC, the H₂O₂ yield rate of G-HTC after the treatment decreased to the similar value in the 2nd cycle. The SEM image of the used G-HTC (Fig. S11a) shows that there are no noticeable changes of the G-HTC morphology after six repeated cycles. Similarly, other structural characterization results including the FT-IR spectra, XRD patterns, and solid-state ¹³C NMR spectra of used G-HTC reveal no obvious differences from those of the initial G-HTC sample (Fig. S11b–d). These results confirm that G-HTC composed of cross-linked furan resin has high physical and chemical stability as a candidate catalyst for the long-term photocatalytic H₂O₂ production. The good long-term stability of G-HTC for H₂O₂ generation will benefit its artificial photosynthesis application. To demonstrate the potential of artificial photosynthesis application of HTCs, G-HTC was used as the catalyst to degrade Rhodamine (RhB) and tetracycline (TC) in photocatalysis and photo-Fenton systems (Fig. S12). The results show that the HTC assisted photo-Fenton system has high performance in pollutant degradation, confirming the high activity of G-HTC in in-situ H₂O₂ generation.

To further verify the functionality of the polyfuran structure in HTC in the photocatalytic H₂O₂ production, the pyrolyzed form of HTC was prepared and tested. The G-HTC was annealed under different temperatures in Ar atmosphere and the prepared samples were denoted as G-HTC-X (X = 250, 300, 350, 400) according to the annealing temperature. As shown in Fig. 3e, with the increase of the annealing temperature, the photocatalytic ability of the pyrolyzed G-HTC samples decreases. The FT-IR spectra of the G-HTC and pyrolyzed G-HTC samples are further compared to study the change in the chemical structure (Fig. S13). The results show that the C–O–C stretching vibration (1302 cm⁻¹), C=C vibration of furanic rings (1510 cm⁻¹), and stretching vibrations of C=O (1701 cm⁻¹) gradually decrease with the increase of the pyrolysis temperature. Considering that C=O is mainly originated from the short keto-aliphatic spacers and levulinic acid [30] rather than the quinone groups linked to the benzene ring, the destruction of the furan motif during the pyrolysis process may be the main reason for the loss of photocatalytic activity. The solid-state ¹³C NMR spectra of G-HTC and G-HTC-350 were further tested (Fig. 3f). For G-HTC, the characteristic peak at 120 ppm and 150 ppm is attributed to O–C=CH- and O–C=CH- site of the furan unit, respectively [30]. The other peaks at 40, 176.5, and 208 ppm can be ascribed to the aliphatic

region (C–H and C–OH), carboxylic acids (–COOH), and ketones (–C=O), respectively [32]. After pyrolysis, the two furan peaks at 120 ppm and 150 ppm disappear and a new peak at 127 ppm from the predominant polyaromatic structure is found. This result further confirms that calcination at higher temperature increases the number of arene units and reduces the amount of furanic groups. The polyfuran units undergo internal rearrangement is also confirmed by the drastic reduction in the oxygen-containing functional group. The thermogravimetry curve of G-HTC is shown in Fig. S14. The G-HTC shows a steep weight loss at > 250 °C, which was attributed to the break of methylene and methylene ether bridges and aromatization of furan. As shown in Fig. S15, the condensation reaction occurs in the polyfuran resin to form 6-membered rings structure containing the inner aromatic rings during the pyrolysis process [17]. The loss in the photocatalytic activity and the structural change of benzenoid-quinoid D-A furan couples clearly indicate that the furan unit in HTC plays a key role in the photocatalytic H₂O₂ production.

3.4. H₂O₂ generation mechanisms

To elucidate the reaction pathways for photocatalytic H₂O₂ generation in the HTC system, the reactive oxygen species (ROS) were first studied by the spin-trapping ESR test. As shown in Fig. 4a, the characteristic peaks assigned to DMPO•O₂ and DMPO•OH were detected for G-HTC under light illumination [59]. These results indicate a dual-channel producing H₂O₂ pathway including photo-reduction of oxygen and photo-oxidation of water in this photocatalytic system [60]. As shown in Fig. 4a, the highly-reactive singlet oxygen (¹O₂), another possible intermediate for H₂O₂ generation, was not detected in the ESR spectra, indicating that ¹O₂ is not involved in the HTC catalyzed H₂O₂ generation process [61].

The quenching experiments were performed to further explore the mechanisms of H₂O₂ photogeneration over the G-HTC catalyst. The AgNO₃, EDTA-2Na, benzoquinone (BQ), and isopropanol (IPA) were selected as scavengers for the electron (e⁻), hole (h⁺), •O₂, and •OH species, respectively (details in Supplementary Data) [62–64]. As shown in Fig. 4b, AgNO₃ can effectively inhibit the production of H₂O₂, indicating that the photogenerated e⁻ transfer on the catalyst surface is a critical step of the reaction. Conversely, EDTA-2Na can react with the photogenerated holes, facilitating the electron transition to the conduction band (CB) and promoting the H₂O₂ generation. For the BQ test, the production of H₂O₂ was significantly suppressed. This indicates that •O₂ played the key role in this photocatalytic oxygen reduction reaction. Besides, the reaction can be enhanced under acidic conditions at pH 3, indicating that the concentration of protons in the solution is another factor determining the H₂O₂ production rate. Considering the above results, the H₂O₂ evolution photoreaction over G-HTC catalyst mainly proceeds by a two-step single-electron reduction (Eqs. (3) and (4)):



Based on the quenching test, IPA has a weak effect on the H₂O₂ production, suggesting that •OH species does not participate in the H₂O₂ generation reaction [65]. However, the •OH signal was detected in the ESR test. Based on the bandgap diagram, the VB position of the G-HTC sample is 1.68 eV, which is lower than the redox potential of + 1.99 eV for •OH/OH⁻ [66]. Thus, it is suggested that •OH is generated through the photo-induced decomposition of H₂O₂ rather than through the water oxidation by the VB holes.

Electrochemical tests using the rotating disk electrode (RDE) method were conducted to study the number of electrons (*n*) involved in the ORR reaction pathway. Fig. S16 shows the linear sweep voltammetry (LSV) curves of G-HTC in an O₂-saturated 0.1 M sodium sulfate electrolyte solution at different rotation speeds. Fig. 4c shows the Koutecky-Levich

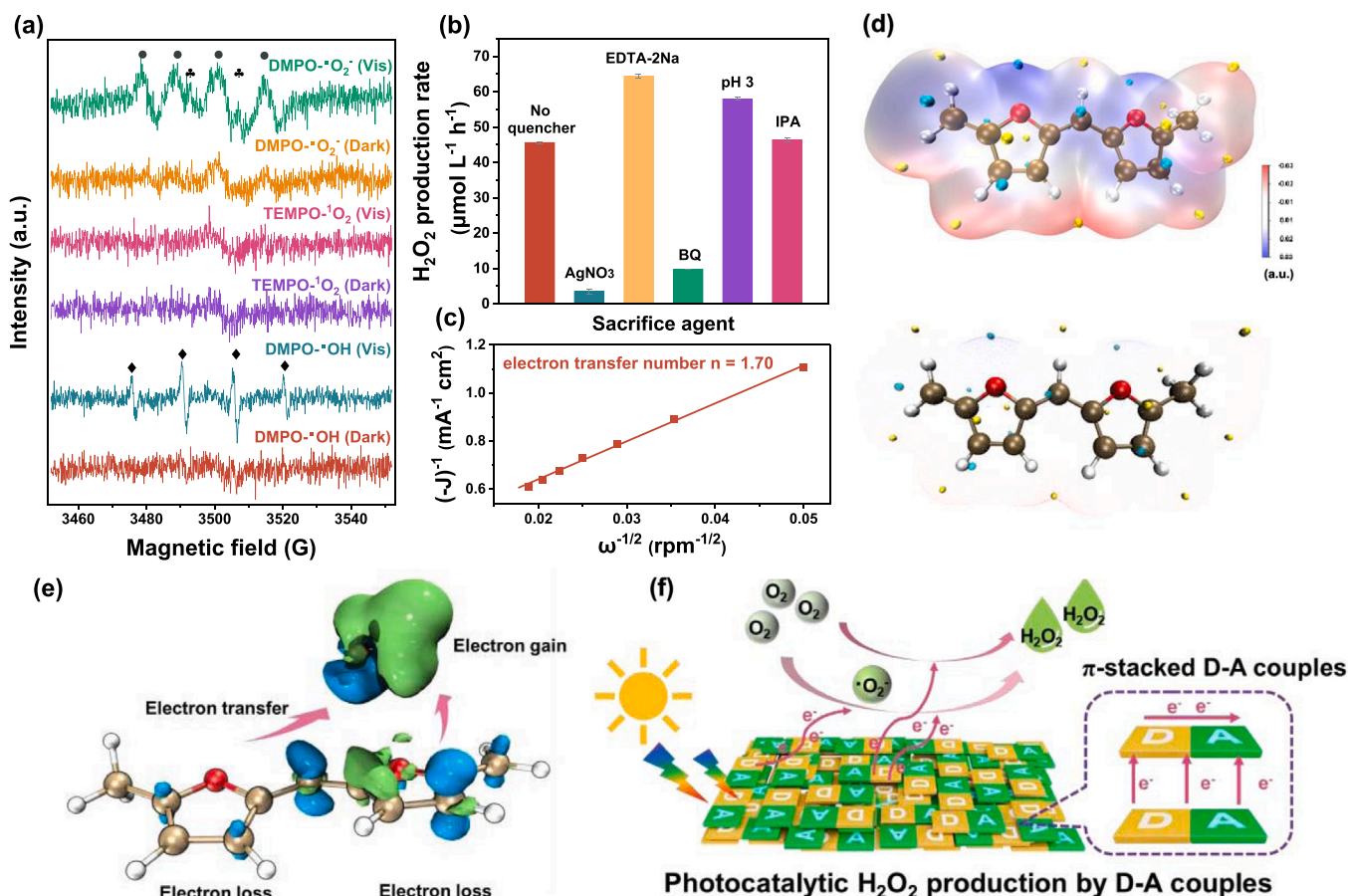


Fig. 4. Reaction mechanism of photocatalytic H₂O₂ production with G-HTC. (a) ESR signals of DMPO-•O₂, DMPO-•OH, and TEMPO-¹O₂ of G-HTC under visible light irradiation. (b) The photocatalytic H₂O₂ production upon the addition of sacrificial agents. For the AgNO₃ experiment, the concentration of H₂O₂ was measured by the titanium potassium oxalate method. Test conditions: water (50 mL), catalyst (5 mg), white LED light (> 420 nm, light intensity: 100 mW cm⁻²). (c) Koutecky-Levich plots of G-HTC obtained from RDE results. (d) Electrostatic potentials of the D-A furan couple. (e) Charge difference map of the O₂ (ads) upon D-A furan couple system. (f) Schematic of the photocatalytic H₂O₂ production mechanism.

plots obtained by the current densities (−1 V vs. SCE) and rotation speed based on the LSV results. The calculated *n* value of the G-HTC, S-HTC, and H-HTC sample is 1.70, 1.78, and 1.70, respectively, indicating that HTC has a mixed one- and two-electron reduction pathway (Eq. (5)) for the H₂O₂ production [67]. Moreover, the *n* values of G-HTC, S-HTC, and H-HTC are similar, indicating that the intrinsic D-A furan units determine the electron transfer characteristics during the ORR process.

The distribution of electrostatic potentials (ESPs) of the D-A furan couple was calculated to study the active sites and the interaction strength in the internal and/or external orientations [68]. As shown in Fig. 4d, the blue and red color shows the negative and positive electrostatic potential, respectively. The positive extreme point (yellow) and negative extreme point (cyan) represent the lowest and the highest electron density, respectively. In the optimized D-A furan model, the highest electron density was found near the oxygen position of each furan monomer. Moreover, considering that the two α-carbons (closest to the oxygen atoms) were connected through the -CH₂ group and C=C bond, this structural unit could serve as the active site for H₂O₂ generation and benefit for the π electron density delocalization through the conjugated D-A furan couple for the enhanced electron transfer.

We further calculated the adsorption energy of O₂ on the acceptor furan model (details in Supplementary Data and Fig. S17). The negative adsorption energy (*E*_{ads}) of −0.11 eV indicates that the adsorption of O₂ on the furan is thermodynamically favorable and is thus beneficial for the H₂O₂ generation [69]. The charge distribution of O₂ adsorption on the D-A furan is shown by the charge density difference map. The charge density difference map was obtained from the charge density differences

between the O₂(ads)-D-A furan and the O₂-D-A furan. As shown in Fig. 4e, the green and blue regions represent the electron accumulation and depletion regions, respectively. Apparently, the O₂ molecule acquires electrons from the penta-cycle of acceptor furan, and the electron transfer occurs from the donor furan to the acceptor furan. The results confirm that O₂(ads) can accept the photogenerated electrons the D-A furan chain for the further photocatalytic H₂O₂ generation.

Based on the experimental and simulation results, the proposed H₂O₂ production mechanism supported by the HTC photocatalysts is shown in Fig. 4f. The HTC semiconductor absorbs the visible light and the generated electrons migrate between the π-conjugation and inter-chain π-stacking D-A furan couples, and eventually diffuse to the catalyst surface. The conduction band electrons (CB e⁻) drive both the two-step single-electron O₂ reduction process via the •O₂ intermediate and the one-step two-electron O₂ reduction process to produce H₂O₂.

3.5. Saccharide and biomass derived HTCs and scaled-up photocatalytic system

In this study, GLU, SUC, and HMF are used as the precursor to prepare HTC, which have similar chemical structures. To further explore the applicability of the HTC catalyst from different precursors, we selected other common carbohydrates to prepare HTCs and investigated their photocatalytic activity in H₂O₂ evolution. As shown in Figs. 5a and S18a, HTCs prepared with fructose (FRU), lactose (LAC), maltose (MAL), cyclodextrin (CYC), and sodium alginate (ALG) as the precursor show high production rates of 205–443 μmol g_{cat}⁻¹ h⁻¹ for photocatalytic H₂O₂

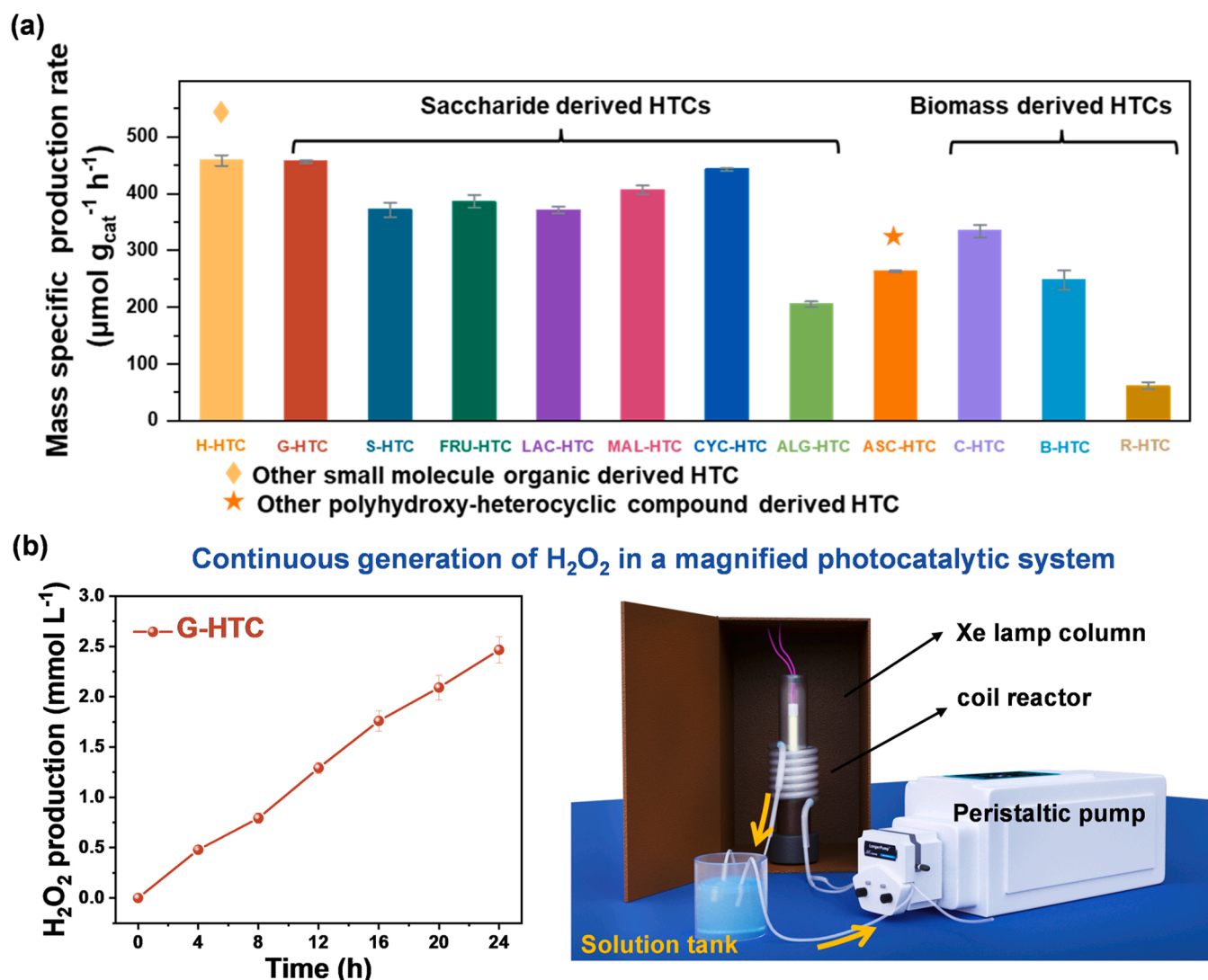


Fig. 5. Saccharide and biomass derived HTCs and continuous generation of H_2O_2 in a scaled-up photocatalytic system. (a) Photocatalytic H_2O_2 production with HTCs synthesized from various precursors. (b) Continuous generation of H_2O_2 by the scaled-up photocatalytic system driven by a peristaltic pump. Test conditions: water (1 L), catalyst (1 g), xenon lamp (light intensity: 34.6 mW cm^{-2}).

generation, which are comparable to those of the G-HTC, S-HTC, and H-HTC. It should be noted that H-HTC with high catalytic activity was synthesized from HMF (a small organic molecule precursor), revealing that saccharides are not the only precursor to synthesize HTC materials. In addition, ASC-HTC prepared from other polyhydroxy-heterocyclic compound, i.e., ascorbic acid (ASC), also possess relatively good H_2O_2 generation performance ($263 \mu\text{mol g}_{\text{cat}}^{-1} \text{h}^{-1}$). The morphology study (Fig. S19) shows that except for HTC prepared from ALG, most of the HTCs exhibit a microsphere-like structure with different particle sizes [28]. The FT-IR spectra (Fig. S18b) of the prepared HTCs from different precursors have similar band signals to those of the G-HTC, S-HTC, and H-HTC samples, which indicates that the HTCs synthesized from saccharides have polyfuran-based skeletons and π -stacked D-A units. Based on the high H_2O_2 generation performance, it is confirmed that various saccharides can be used to produce highly-efficient HTC catalysts for photocatalytic H_2O_2 production.

Considering that the G-HTC sample has a high H_2O_2 generation performance, cellulose (a biopolymer composed of glucose monomers, one of the three key components of biomass), may also be used to produce HTC [70]. To investigate the possibility of using biomass waste to produce H_2O_2 photocatalysts, cellulose, bean straw, and rice straw were further used as the raw precursor materials to produce HTCs. As shown

in Figs. 5a and S20, the HTCs produced from cellulose (C-HTC) and bean straw (B-HTC) precursors also have good H_2O_2 production performance and similar furan structures. This result indicates that abundant biomass waste can be converted to inexpensive, metal-free, and efficient HTC photocatalysts for photo-chemical H_2O_2 production.

A previous study reported a H_2O_2 production photocatalyst based on the hydrothermal carbons produced by saccharides, cellulose, and biomass wastes. Compared with this study, in our work, we experimentally show that the unique structure with conjugated furan pairs linked through $-\text{CH}_2$ group and C double bond (D-A structure) is the key unit contributes to the high photoactivity, which was not mentioned or investigated in the reported paper. Moreover, as we discussed, HMF is an important intermediate and product in the hydrothermal reaction of saccharides. It is the “seed precursor” to produce hydrothermal carbons, which means no matter what biomass or precursors that being used, if the HMF is produced during the reaction, the final product of hydrothermal carbons may have that D-A furan structure and high photocatalytic activity. Our experiment with the HMF as the precursor confirmed this hypothesis by the fact the H-HTC has high H_2O_2 production rate (Fig. 5a). Thus, our study presents a deeper understanding on the D-A structure in hydrothermal carbons and the relationship between this structural unit and photocatalytic activity. The novelty of our

study compared with the reported work was shown in Table S5.

Current H₂O₂ photo-chemical production systems are commonly based on batch reactors with relatively small capacity [14,71]. Herein, we innovatively design a spiral photocatalytic flow reactor (as shown in Fig. 5b) to study the performance of HTC for the continuous-cycle H₂O₂ photocatalytic production. This system achieves efficient irradiation and thorough solid-gas-liquid triphasic mixing, which is particularly suitable for long-term operation. This scaled-up system (1 L reactor) with the G-HTC as the catalyst produces 2.464 mM H₂O₂ after 24 h of operation.

4. Conclusion

This study has demonstrated the novel furan-resin-carbons synthesized by hydrothermal carbonization as highly-efficient photocatalysts for H₂O₂ production. The π -stacked D-A units in the furan polymer chain lead to a narrow HTC bandgap (~ 2.0 eV), which enables the O₂ reduction to produce H₂O₂ through the effective photoelectron absorb under solar irradiation. The mechanism study reveals that the photo-chemical H₂O₂ evolution reaction over the G-HTC catalyst proceeds through mixed one- and two-electron reduction pathway. Considering the current challenges for real-world applications of photocatalytic H₂O₂ evolution, HTC, as a new type of photocatalyst, provides the following novel and innovative solutions:

- (i) highly-efficient H₂O₂ production under ambient conditions without any commonly used sacrificial agents and O₂ aeration;
- (ii) low-cost and metal-free catalyst synthesized from a broad range of raw precursor materials including biomass wastes; and
- (iii) significantly enhanced H₂O₂ production through custom-designed system and light source.

Collectively, these new findings contribute to the development of next-generation advanced metal-free, carbon-based photocatalysts for H₂O₂ generation and open new opportunities for biomass waste utilization.

CRediT authorship contribution statement

Wei Miao: Conceptualization, Data curation, Formal analysis, Investigation, Methodology, Validation, Writing – original draft. **Ducheng Yao:** Data curation, Formal analysis, Investigation, Methodology. **Chengcheng Chu:** Data curation, Formal analysis, Investigation, Methodology. **Ying Liu:** Data curation, Formal analysis, Investigation, Methodology. **Qisu Huang:** Data curation, Formal analysis, Investigation, Methodology. **Shun Mao:** Conceptualization, Investigation, Project administration, Supervision, Writing – review & editing. **Kostya (Ken) Ostrikov:** Investigation, Writing – review & editing.

Declaration of Competing Interest

The authors declare that they have no known competing financial interests or personal relationships that could have appeared to influence the work reported in this paper.

Data availability

Data will be made available on request.

Acknowledgments

This work was supported by the National Key R&D Program of China (2019YFC1905400) and the Fundamental Research Funds for the Central Universities (2022-4-ZD-08). K.O. thanks the Australian Research Council and QUT Centre for Materials Science for partial support.

Appendix A. Supplementary material

Supplementary data associated with this article can be found in the online version at doi:10.1016/j.apcatb.2023.122770.

References

- [1] C. Xia, Y. Xia, P. Zhu, L. Fan, H. Wang, Direct electrosynthesis of pure aqueous H₂O₂ solutions up to 20% by weight using a solid electrolyte, *Science* 366 (2019) 226.
- [2] J.M. Campos-Martin, G. Blanco-Brieva, J.L.G. Fierro, Hydrogen peroxide synthesis: an outlook beyond the anthraquinone process, *Angew. Chem. Int. Ed.* 45 (2006) 6962–6984.
- [3] X. Hu, X. Zeng, Y. Liu, J. Lu, X. Zhang, Carbon-based materials for photo- and electrocatalytic synthesis of hydrogen peroxide, *Nanoscale* 12 (2020) 16008–16027.
- [4] C. Chu, Q. Li, W. Miao, H. Qin, X. Liu, D. Yao, S. Mao, Photocatalytic H₂O₂ production driven by cyclodextrin-pyrimidine polymer in a wide pH range without electron donor or oxygen aeration, *Appl. Catal. B Environ.* 314 (2022), 121485.
- [5] Y. Zheng, L. Lin, B. Wang, X. Wang, Graphitic carbon nitride polymers toward sustainable photoredox catalysis, *Angew. Chem. Int. Ed.* 54 (2015) 12868–12884.
- [6] X. Wang, S. Blechert, M. Antonietti, Polymeric graphitic carbon nitride for heterogeneous photocatalysis, *ACS Catal.* 2 (2012) 1596–1606.
- [7] C. Chu, W. Miao, Q. Li, D. Wang, Y. Liu, S. Mao, Highly efficient photocatalytic H₂O₂ production with cyano and SnO₂ co-modified g-C₃N₄, *Chem. Eng. J.* 428 (2022), 132531.
- [8] H. Fattahimoghaddam, T. Mahvelati-Shamsabadi, C.-S. Jeong, B.-K. Lee, Coral-like potassium and phosphorous doped graphitic carbon nitride structures with enhanced charge and mass transfer dynamics toward photocatalytic hydrogen peroxide production and microbial disinfection, *J. Colloid Interface Sci.* 617 (2022) 326–340.
- [9] X. Zeng, Y. Liu, X. Hu, X. Zhang, Photoredox catalysis over semiconductors for light-driven hydrogen peroxide production, *Green Chem.* 23 (2021) 1466–1494.
- [10] H. Hou, X. Zeng, X. Zhang, Production of hydrogen peroxide by photocatalytic processes, *Angew. Chem. Int. Ed.* 59 (2020) 17356–17376.
- [11] Y. Shiraishi, T. Takii, T. Hagi, S. Mori, Y. Kofuji, Y. Kitagawa, S. Tanaka, S. Ichikawa, T. Hirai, Resorcinol-formaldehyde resins as metal-free semiconductor photocatalysts for solar-to-hydrogen peroxide energy conversion, *Nat. Mater.* 18 (2019) 985–993.
- [12] H.A.M. van Mullekom, J.A.J.M. Vekemans, E.E. Havinga, E.W. Meijer, Developments in the chemistry and band gap engineering of donor-acceptor substituted conjugated polymers, *Mater. Sci. Eng. R Rep.* 32 (2001) 1–40.
- [13] Y.-J. Cheng, S.-H. Yang, C.-S. Hsu, Synthesis of conjugated polymers for organic solar cell applications, *Chem. Rev.* 109 (2009) 5868–5923.
- [14] Y. Shiraishi, M. Matsumoto, S. Ichikawa, S. Tanaka, T. Hirai, Polythiophene-doped resorcinol-formaldehyde resin photocatalysts for solar-to-hydrogen peroxide energy conversion, *J. Am. Chem. Soc.* 143 (2021) 12590–12599.
- [15] Y. Hou, F. Liu, B. Zhang, M. Tong, Thiadiazole-based covalent organic frameworks with a donor-acceptor structure: modulating intermolecular charge transfer for efficient photocatalytic degradation of typical emerging contaminants, *Environ. Sci. Technol.* 56 (2022) 16303–16314.
- [16] Z. Hu, G. Liu, X. Chen, Z. Shen, J.C. Yu, Enhancing charge separation in metallic photocatalysts: a case study of the conducting molybdenum dioxide, *Adv. Funct. Mater.* 26 (2016) 4445–4455.
- [17] C. Falco, F. Perez Caballero, F. Babonneau, C. Gervais, G. Laurent, M.-M. Titirici, N. Baccile, Hydrothermal carbon from biomass: structural differences between hydrothermal and pyrolyzed carbons via 13C solid state NMR, *Langmuir* 27 (2011) 14460–14471.
- [18] Z. Hu, Z. Shen, J.C. Yu, Converting carbohydrates to carbon-based photocatalysts for environmental treatment, *Environ. Sci. Technol.* 51 (2017) 7076–7083.
- [19] L. Xu, Y. Liu, Z. Hu, J.C. Yu, Converting cellulose waste into a high-efficiency photocatalyst for Cr(VI) reduction via molecular oxygen activation, *Appl. Catal. B Environ.* 295 (2021), 120253.
- [20] C. Falco, N. Baccile, M.-M. Titirici, Morphological and structural differences between glucose, cellulose and lignocellulosic biomass derived hydrothermal carbons, *Green Chem.* 13 (2011) 3273–3281.
- [21] L.J.R. Higgins, A.P. Brown, J.P. Harrington, A.B. Ross, B. Kaulich, B. Mishra, Evidence for a core-shell structure of hydrothermal carbon, *Carbon* 161 (2020) 423–431.
- [22] T. Marszałek, M. Li, W. Pisula, Design directed self-assembly of donor-acceptor polymers, *Chem. Commun.* 52 (2016) 10938–10947.
- [23] L. Xu, Y. Liu, L. Li, Z. Hu, J.C. Yu, Fabrication of a photocatalyst with biomass waste for H₂O₂ synthesis, *ACS Catal.* 11 (2021) 14480–14488.
- [24] Y.-X. Ye, J. Pan, F. Xie, L. Gong, S. Huang, Z. Ke, F. Zhu, J. Xu, G. Ouyang, Highly efficient photosynthesis of hydrogen peroxide in ambient conditions, *Proc. Natl. Acad. Sci. USA* 118 (2021), e2103964118.
- [25] L. Chen, L. Wang, Y. Wan, Y. Zhang, Z. Qi, X. Wu, H. Xu, Acetylene and diacetylene functionalized covalent triazine frameworks as metal-free photocatalysts for hydrogen peroxide production: a new two-electron water oxidation pathway, *Adv. Mater.* 32 (2020), 1904433.
- [26] M. Teranishi, S.-i. Naya, H. Tada, In situ liquid phase synthesis of hydrogen peroxide from molecular oxygen using gold nanoparticle-loaded titanium(IV) dioxide photocatalyst, *J. Am. Chem. Soc.* 132 (2010) 7850–7851.

- [27] Z. Teng, Q. Zhang, H. Yang, K. Kato, W. Yang, Y.-R. Lu, S. Liu, C. Wang, A. Yamakata, C. Su, B. Liu, T. Ohno, Atomically dispersed antimony on carbon nitride for the artificial photosynthesis of hydrogen peroxide, *Nat. Catal.* 4 (2021) 374–384.
- [28] Q. He, Y. Yu, J. Wang, X. Suo, Y. Liu, Kinetic study of the hydrothermal carbonization reaction of glucose and its product structures, *Ind. Eng. Chem. Res.* 60 (2021) 4552–4561.
- [29] Y. Qi, M. Zhang, L. Qi, Y. Qi, Mechanism for the formation and growth of carbonaceous spheres from sucrose by hydrothermal carbonization, *RSC Adv.* 6 (2016) 20814–20823.
- [30] N. Baccile, G. Laurent, F. Babonneau, F. Fayon, M.-M. Titirici, M. Antonietti, Structural characterization of hydrothermal carbon spheres by advanced solid-state MAS 13C NMR investigations, *J. Phys. Chem. C* 113 (2009) 9644–9654.
- [31] C. Dai, B. Liu, Conjugated polymers for visible-light-driven photocatalysis, *Energy Environ. Sci.* 13 (2020) 24–52.
- [32] M. Sevilla, A.B. Fuentès, Chemical and structural properties of carbonaceous products obtained by hydrothermal carbonization of saccharides, *Chem. Eur. J.* 15 (2009) 4195–4203.
- [33] J. Ryu, Y.-W. Suh, D.J. Suh, D.J. Ahn, Hydrothermal preparation of carbon microspheres from mono-saccharides and phenolic compounds, *Carbon* 48 (2010) 1990–1998.
- [34] G. Patrinoiu, J.M. Calderon-Moreno, R. Birjega, O. Carp, Solid vs. hollow oxide spheres obtained by hydrothermal carbonization of various types of carbohydrates, *RSC Adv.* 5 (2015) 31768–31771.
- [35] M.-M. Titirici, A. Thomas, M. Antonietti, Aminated hydrophilic ordered mesoporous carbons, *J. Mater. Chem.* 17 (2007) 3412–3418.
- [36] Y. Shiraishi, T. Hagi, M. Matsumoto, S. Tanaka, S. Ichikawa, T. Hirai, Solar-to-hydrogen peroxide energy conversion on resorcinol–formaldehyde resin photocatalysts prepared by acid-catalysed polycondensation, *Commun. Chem.* 3 (2020) 169.
- [37] S. Li, F. Liang, J. Wang, H. Zhang, S. Zhang, Preparation of mono-dispersed carbonaceous spheres via a hydrothermal process, *Adv. Powder Technol.* 28 (2017) 2648–2657.
- [38] S. Kuroda, T. Noguchi, T. Ohnishi, Electron nuclear double resonance observation of π -electron defect states in undoped poly(paraphenylene vinylene), *Phys. Rev. Lett.* 72 (1994) 286–289.
- [39] L. Shi, L. Yang, W. Zhou, Y. Liu, L. Yin, X. Hai, H. Song, J. Ye, Photoassisted construction of hole defective g-C₃N₄ photocatalysts for efficient visible-light-driven H₂O₂ production, *Small* 14 (2018), 1703142.
- [40] M. Teranishi, S.-i. Naya, H. Tada, In situ liquid phase synthesis of hydrogen peroxide from molecular oxygen using gold nanoparticle-loaded titanium(IV) dioxide photocatalyst, *J. Am. Chem. Soc.* 132 (2010) 7850–7851.
- [41] Z. Zhu, H. Pan, M. Murugananthan, J. Gong, Y. Zhang, Visible light-driven photocatalytically active g-C₃N₄ material for enhanced generation of H₂O₂, *Appl. Catal. B Environ.* 232 (2018) 19–25.
- [42] S. Li, G. Dong, R. Hailili, L. Yang, Y. Li, F. Wang, Y. Zeng, C. Wang, Effective photocatalytic H₂O₂ production under visible light irradiation at g-C₃N₄ modulated by carbon vacancies, *Appl. Catal. B Environ.* 190 (2016) 26–35.
- [43] J. Zhang, J. Lang, Y. Wei, Q. Zheng, L. Liu, Y.-H. Hu, B. Zhou, C. Yuan, M. Long, Efficient photocatalytic H₂O₂ production from oxygen and pure water over graphitic carbon nitride decorated by oxidative red phosphorus, *Appl. Catal. B Environ.* 298 (2021), 120522.
- [44] C. Chu, Q. Zhu, Z. Pan, S. Gupta, D. Huang, Y. Du, S. Weon, Y. Wu, C. Muhich, E. Stavitski, K. Domen, J.-H. Kim, Spatially separating redox centers on 2D carbon nitride with cobalt single atom for photocatalytic production, *Proc. Natl. Acad. Sci. USA* 117 (2020) 6376.
- [45] L. Wang, S. Cao, K. Guo, Z. Wu, Z. Ma, L. Piao, Simultaneous hydrogen and peroxide production by photocatalytic water splitting, *Chin. J. Catal.* 40 (2019) 470–475.
- [46] R. Ma, L. Wang, H. Wang, Z. Liu, M. Xing, L. Zhu, X. Meng, F.-S. Xiao, Solid acids accelerate the photocatalytic hydrogen peroxide synthesis over a hybrid catalyst of titania nanotube with carbon dot, *Appl. Catal. B Environ.* 244 (2019) 594–603.
- [47] M. Kou, Y. Wang, Y. Xu, L. Ye, Y. Huang, B. Jia, H. Li, J. Ren, Y. Deng, J. Chen, Y. Zhou, K. Lei, L. Wang, W. Liu, H. Huang, T. Ma, Molecularly engineered covalent organic frameworks for hydrogen peroxide photosynthesis, *Angew. Chem. Int. Ed.* 61 (2022), e202200413.
- [48] M.I. Cabrera, O.M. Alfano, A.E. Cassano, Absorption and scattering coefficients of titanium dioxide particulate suspensions in water, *J. Phys. Chem. C* 100 (1996) 20043–20050.
- [49] I. Grčić, G. Li, Puma, Six-flux absorption-scattering models for photocatalysis under wide-spectrum irradiation sources in annular and flat reactors using catalysts with different optical properties, *Appl. Catal. B Environ.* 211 (2017) 222–234.
- [50] H. Yu, R. Shi, Y. Zhao, T. Bian, Y. Zhao, C. Zhou, G.I.N. Waterhouse, L.-Z. Wu, C.-H. Tung, T. Zhang, Alkali-assisted synthesis of nitrogen deficient graphitic carbon nitride with tunable band structures for efficient visible-light-driven hydrogen evolution, *Adv. Mater.* 29 (2017), 1605148.
- [51] D. Wang, Q. Li, W. Miao, Y. Liu, N. Du, S. Mao, One-pot synthesis of ultrafine NiO loaded and Ti³⁺ in-situ doped TiO₂ induced by cyclodextrin for efficient visible-light photodegradation of hydrophobic pollutants, *Chem. Eng. J.* 402 (2020), 126211.
- [52] J. Zhang, B. Jing, Z. Tang, Z. Ao, D. Xia, M. Zhu, S. Wang, Experimental and DFT insights into the visible-light driving metal-free C₃N₅ activated persulfate system for efficient water purification, *Appl. Catal. B Environ.* 289 (2021), 120023.
- [53] S. Manzetti, T. Lu, Alternant conjugated oligomers with tunable and narrow HOMO–LUMO gaps as sustainable nanowires, *RSC Adv.* 3 (2013) 25881–25890.
- [54] D. Wang, M.A. Mueses, J.A.C. Márquez, F. Machuca-Martínez, I. Grčić, R. Peralta Muniz Moreira, G. Li Puma, Engineering and modeling perspectives on photocatalytic reactors for water treatment, *Water Res.* 202 (2021), 117421.
- [55] R. Acosta-Herazo, M.A. Mueses, G.L. Puma, F. Machuca-Martínez, Impact of photocatalyst optical properties on the efficiency of solar photocatalytic reactors rationalized by the concepts of initial rate of photon absorption (IRPA) dimensionless boundary layer of photon absorption and apparent optical thickness, *Chem. Eng. J.* 356 (2019) 839–849.
- [56] M. Saldaña, B. Serrano, H.L. de Lasa, Experimental evaluation of photon absorption in an aqueous TiO₂ slurry reactor, *Chem. Eng. J.* 90 (2002) 219–229.
- [57] D. Dolat, N. Quici, E. Kusiak-Nejman, A.W. Morawski, G. Li Puma, One-step, hydrothermal synthesis of nitrogen, carbon co-doped titanium dioxide (N,C-TiO₂) photocatalysts. Effect of alcohol degree and chain length as carbon dopant precursors on photocatalytic activity and catalyst deactivation, *Appl. Catal. B Environ.* 115–116 (2012) 81–89.
- [58] N. Chen, Y. Huang, X. Hou, Z. Ai, L. Zhang, Photochemistry of hydrochar: reactive oxygen species generation and sulfadiazine degradation, *Environ. Sci. Technol.* 51 (2017) 11278–11287.
- [59] W. Miao, Y. Liu, X. Chen, Y. Zhao, S. Mao, Tuning layered Fe-doped g-C₃N₄ structure through pyrolysis for enhanced Fenton and photo-Fenton activities, *Carbon* 159 (2020) 461–470.
- [60] Y. Zhao, Y. Liu, J. Cao, H. Wang, M. Shao, H. Huang, Y. Liu, Z. Kang, Efficient production of H₂O₂ via two-channel pathway over ZIF-8/C₃N₄ composite photocatalyst without any sacrificial agent, *Appl. Catal. B Environ.* 278 (2020), 119289.
- [61] S. Zhao, X. Zhao, Insights into the role of singlet oxygen in the photocatalytic hydrogen peroxide production over polyoxometalates-derived metal oxides incorporated into graphitic carbon nitride framework, *Appl. Catal. B Environ.* 250 (2019) 408–418.
- [62] Q. Wu, J. Cao, X. Wang, Y. Liu, Y. Zhao, H. Wang, Y. Liu, H. Huang, F. Liao, M. Shao, Z. Kang, A metal-free photocatalyst for highly efficient hydrogen peroxide photoproduction in real seawater, *Nat. Commun.* 12 (2021) 483.
- [63] W. Lu, T. Xu, Y. Wang, H. Hu, N. Li, X. Jiang, W. Chen, Synergistic photocatalytic properties and mechanism of g-C₃N₄ coupled with zinc phthalocyanine catalyst under visible light irradiation, *Appl. Catal. B Environ.* 180 (2016) 20–28.
- [64] W. Miao, Y. Wang, Y. Liu, H. Qin, C. Chu, S. Mao, Persulfate-induced three coordinate nitrogen (N₃C) vacancies in defective carbon nitride for enhanced photocatalytic H₂O₂ evolution, *Engineering* (2022), <https://doi.org/10.1016/j.eng.2021.12.016>.
- [65] L. Yang, G. Dong, D.L. Jacobs, Y. Wang, L. Zang, C. Wang, Two-channel photocatalytic production of H₂O₂ over g-C₃N₄ nanosheets modified with perylene imides, *J. Catal.* 352 (2017) 274–281.
- [66] X. Wang, Z. Han, L. Yu, C. Liu, Y. Liu, G. Wu, Synthesis of full-spectrum-response Cu₂(OH)PO₄/g-C₃N₄ photocatalyst with outstanding photocatalytic H₂O₂ production performance via a “Two Channel Route”, *ACS Sustain. Chem. Eng.* 6 (2018) 14542–14553.
- [67] Y. Xie, Y. Li, Z. Huang, J. Zhang, X. Jia, X.-S. Wang, J. Ye, Two types of cooperative nitrogen vacancies in polymeric carbon nitride for efficient solar-driven H₂O₂ evolution, *Appl. Catal. B Environ.* 265 (2020), 118581.
- [68] D. Habibi, A.R. Faraji, D. Sheikh, M. Sheikh, S. Abedi, Application of supported Mn (iii), Fe(iii) and Co(ii) as heterogeneous, selective and highly reusable nano catalysts for synthesis of arylaminotetrazoles, and DFT studies of the products, *RSC Adv.* 4 (2014) 47625–47636.
- [69] Y. Hu, P. Zhang, J. Du, C. Kim, S. Han, W. Choi, Bifunctional carbon nitride exhibiting both enhanced photoactivity and residual catalytic activity in the post-irradiation dark period, *ACS Catal.* 11 (2021) 14941–14955.
- [70] A.C. O’Sullivan, Cellulose: the structure slowly unravels, *Cellulose* 4 (1997) 173–207.
- [71] J. Cao, H. Wang, Y. Zhao, Y. Liu, Q. Wu, H. Huang, M. Shao, Y. Liu, Z. Kang, Phosphorus-doped porous carbon nitride for efficient sole production of hydrogen peroxide via photocatalytic water splitting with a two-channel pathway, *J. Mater. Chem. A* 8 (2020) 3701–3707.